Journal of Road Engineering 3 (2023) 300–314

Contents lists available at ScienceDirect

Journal of Road Engineering

journal homepage: www.keaipublishing.com/en/journals/journal-of-road-engineering

Original Article

Virtual strain loading method for low temperature cohesive failure of asphalt binder

Heyang Ding [a,b], Hainian Wang [a,*], Ziye Ma [a,c], Zhen Leng [d], Ponan Feng [a], Tangjie Wang [a], Xin Qu [a]

[a] School of Highway, Chang'an University, Xi'an 710064, China
[b] Institute of Highway Engineering, RWTH Aachen University, Aachen D52074, Germany
[c] Department of Civil and Architectural Engineering, KTH Royal Institute of Technology, Stockholm 10044, Sweden
[d] Department of Civil and Environmental Engineering, The Hong Kong Polytechnic University, Hong Kong, China

HIGHLIGHTS

- The tetragonal asphalt binder model was constructed based on molecular dynamics simulations.
- The critical separation strain is hardly influenced by strain loading combinations.
- Increasing strain rate significantly enhanced the maximum traction stress and separation work.
- The strain combination of 0.5%-80 provided a more accurate representation of the actual asphalt's tensile behavior trend.

ARTICLE INFO

Keywords:
Asphalt binder
Cohesive failure
Virtual strain load
Molecular dynamics
Maximum cohesive stress

ABSTRACT

Cohesive failure is one of the primary reasons for low-temperature cracking in asphalt pavements. Understanding the micro-level mechanism is crucial for comprehending cohesive failure behavior. However, previous literature has not fully reported on this aspect. Moreover, there has been insufficient attention given to the correlation between macroscopic and microscopic failures. To address these issues, this study employed molecular dynamics simulation to investigate the low-temperature tensile behavior of asphalt binder. By applying virtual strain, the separation work during asphalt binder tensile failure was calculated. Additionally, a correlation between macroscopic and microscopic tensile behaviors was established. Specifically, a quadrilateral asphalt binder model was generated based on SARA fractions. By applying various combinations of virtual strain loading, the separation work at tensile failure was determined. Furthermore, the impact of strain loading combinations on separation work was analyzed. Normalization was employed to establish the correlation between macroscopic and microscopic tensile behaviors. The results indicated that thermodynamic and classical mechanical indicators validated the reliability of the tetragonal asphalt binder model. The strain loading combination consists of strain rate and loading number. All strain loading combinations exhibited the similar tensile failure characteristic. The critical separation strain was hardly influenced by strain loading combination. However, increasing strain rate significantly enhanced both the maximum traction stress and separation work of the asphalt binder. An increment in the loading number led to a decrease in separation work. The virtual strain combination of 0.5%-80 provided a more accurate representation of the actual asphalt's tensile behavior trend.

---

* Corresponding author.
E-mail addresses: dingheyang@chd.edu.cn (H. Ding), wanghn@chd.edu.cn (H. Wang), zyma@chd.edu.cn (Z. Ma), zhen.leng@polyu.edu.hk (Z. Leng), fpn460@hotmail.com (P. Feng), 1812138977@qq.com (T. Wang), quxin@chd.edu.cn (X. Qu).

Peer review under responsibility of Chang'an University.

https://doi.org/10.1016/j.jreng.2022.09.004
Received 9 January 2022; Received in revised form 7 September 2022; Accepted 9 September 2022

1. Introduction

There are two primary types of damage that are most important in asphalt mixtures: adhesive failure and cohesive failure. Adhesive failure occurs at the aggregate surface and is primarily due to insufficient interfacial adhesion strength. On the other hand, cohesive failure takes place within the asphalt binder itself and is characterized by a lack of cohesive strength. It is worth noting that there is often no strict division between these two failure forms. Additionally, environmental factors such as temperature, moisture and load form can have an impact on the specific failure form to asphalt mixture (Gong et al., 2021; Ramezani and Rickgauer, 2020; Tan and Guo, 2013; Yuan et al., 2020).

Adhesive failure of asphalt binder has been a prominent research topic in road engineering for an extended period. The emergence and advancement of Molecular Dynamics (MD) simulations have allowed investigation of adhesion damage at the Ångstrom (Å, 1 Å $= 10^{-10}$ m) -picosecond (ps, 1 ps $= 10^{-12}$ s) range. MD offers the advantage of precise energy analysis, which has led to the exploration of interfacial adhesion work in asphalt binder-aggregate interface properties (Wang et al., 2020a).

Essentially, the concept of interfacial adhesion work extends from the idea of interaction energy. Xu and Wang (2016b) observed that the interfacial interaction energy of asphalt binder-aggregate is notably influenced by the type of aggregate. For instance, the interaction energy of the same asphalt binder on the silica surface was 30%–40% lower than on the calcite surface. The main driving forces for the interaction energy at the interface were van der Waals and electrostatic forces (Feng et al., 2020). Variations in the atomic arrangement of aggregate surfaces, including aggregate type and surface crystal orientation, have a significant impact on the interfacial interaction energy and internal driving sources.

The interfacial interaction energy at the quartz surface is predominantly dominated by van der Waals force, with the effect of electrostatic force being suppressed (Gao et al., 2018; Liu et al., 2020). On alkaline mineral surfaces, such as calcite (Ding et al., 2020; Gao et al., 2018; Luo et al., 2020), albite (Feng et al., 2020; Gao et al., 2018), and microcline (Gao et al., 2018), the percent of the electrostatic force in interfacial interaction energy increases and even becomes the main driver of the interfacial interaction energy. The crystallographic orientation of the aggregate surface is another manifestation of the differences in the atomic arrangement. Compared to quartz (0, 0, 1), Feng et al. (2020) reported a 40% higher van der Waals force strength for quartz (0, 1, 0), and Chu et al. (2019) reported a 32% higher van der Waals force for quartz (1, 0, 1). In the case of albite surfaces, electrostatic forces mainly constitute the interfacial interactions at albite (0, 0, 1) surfaces, whereas van der Waals force is the primary driving source for interfacial interaction energy at albite (0, 1, 0) surfaces (Feng et al., 2020).

Another approach to investigate the interface properties of asphalt mixtures is the microscopic dynamic mechanical model. By recording the internal stresses at each tensile strain, the maximum interfacial strength can be obtained during the tensile process of the two-phase materials. Strain rate, model size, and temperature are considered to be potential factors influencing the maximum interfacial strength. The results of Wang et al. (2017) showed that the maximum interfacial strength of the asphalt binder-aggregate model did not have a dependence on strain rate. Xu and Wang (2016a) applied strain rates of 10, 20, and 30 m/s to the asphalt binder-aggregate model. The maximum interfacial strength varied to some extent at different strain rates. However, these variations were not significant enough to support the idea that there exists a strain rate dependence on the maximum interfacial strength in the asphalt binder-aggregate model.

The main approach to analyzing cohesive failure in asphalt binder using the MD method is through direct tensile simulation (i.e., a mode of mechanical application). Sun and Wang (2020a) concluded that cohesive failure in asphalt binder started with nanoscale cavities. As the tensile progressed, the nanoscale cavities connected and eventually formed cracks through asphalt binder. Du and Zhu (2019) and Du et al. (2021) proposed that cohesion failure occurs at low strain rate, while adhesion failure occurs at a high strain rate. However, it was observed that the maximum separation stress (i.e., the maximum interfacial strength and cohesive strength) still does not have a dependence on the strain rate in the same form of failure. The results reported by Wang et al. (2017) indicated a non-negligible effect of mechanical model size on the calculation of maximum interfacial strength (i.e., size effect).

However, Du et al. (2021) do not agree with the previous conclusions. The molecular weight of the asphalt binder-aggregate model constructed by Du et al. (2021) is twice as large as that of Wang et al. (2017). Thus, the size effect can be assumed to have been eliminated. Increasing the number of atoms involved in simulations is an effective way to eliminate the size effect. In addition, the simulation results for the temperature variate showed that the maximum interfacial strength tends to be negatively correlated with temperature (Wang et al., 2017; Xu and Wang, 2016a).

It is worth noting that in the asphalt binder-aggregate model, cohesive failure was observed only within a range of 10 Å to 50 Å from the aggregate surface. Such proximity to the aggregate surface is insufficient to classify it as cohesive failure; this type of failure mode is still considered as interface failure.

Therefore, the research and development of new cohesive failure model is crucially necessary. However, related research work has not been carried out extensively. In this article, the tetragonal asphalt binder model was constructed as an analytical object for asphalt binder cohesive damage. Based on the virtual strain loading method, the traction stress-cumulative strain curves of asphalt binder were obtained and the influence of load parameters was further analyzed. The correlation between the virtual strain loading method and the real direct tensile test was established with reference to universal testing machines (UTM) test results.

2. Experiment and simulation methodology

2.1. Asphalt binder cohesion failure test based on UTM system

In this article, UTM combined with fracture energy test (BFE) was used to obtain the cohesive damage characteristics of asphalt binder during the direct tension process. The UTM system can be used in environments from −20 °C to 60 °C with the loading force of 30 kN to meet a wide range of asphalt binder tensile properties test methods such as AASHTO T 314-12 (DT), AASHTO TP 113-15 (DENT) and TP 127-17 (BFE).

This article used the BFE method (AASHTO TP 127-17) incorporated into the AASHTO system for asphalt binder tensile testing. The BFE test method performs tensile testing of asphalt binder in the range of 0 °C–25 °C. The geometry of the specimen was designed to introduce sufficient stress concentration in the middle of the specimen to allow the fracture to occur. Before the tensile test, the spacing between the loading ends of UTM system was adjusted to meet the loading requirements of the asphalt binder specimen, the upper loading end is moved at a constant tensile rate while the lower loading end is held constant, the upper loading end is pulled (the lower end remains fixed) and the test is performed, the tensile displacement and load data are recorded until fracture occurs. The test specimens were cast and cooled in compliant molds in accordance with AASHTO T 40-02 and AASHTO TP 127-17. After completion of the asphalt binder forming process, asphalt binder specimens were hung between lower-end and upper-end by adjusting the distance of load ends. It is important to note that the data generated by the UTM system is acquired and processed differently in this article from the requirements of the original specification (i.e., AASHTO TP 127-17). This article began by running the tensile process with a zero-load to obtain blank noise data. Blank noise data will be excluded from the formal asphalt specimen tensile test. To match the loading and acquisition method of the traction stress in the virtual tensile process, this article obtained the correspondence between actuator deformation-traction stress by loading the upper-end.

Table 1
The weight ratio of different fractions in asphalt binder.

Fraction		Number	Weight (%)
Asphaltene (Asp)	Asp-1	6	17.8
	Asp-2	4	
	Asp-3	8	
Saturate (Sa)	Sa-1	14	15.5
	Sa-2	14	
Aromatic (Ar)	Ar-1	36	41.4
	Ar-2	42	
Resin (Re)	Re-1	4	25.3
	Re-2	4	
	Re-3	6	
	Re-4	4	
	Re-5	30	

The UTM system was designed for an ambient temperature of 10 °C and a traction rate of 200 mm/min. The operational procedures and other parameters not mentioned in this article were in accordance with AASHTO TP 127-17.

2.1. Molecular structure of asphalt binder cohesion failure model

The representative molecular structures of the different components are based on the results of Martín-Martínez et al. (2015) and Li and Greenfield (2014). The choice of representative molecular structures is in line with those adopted by other different research institutes and personnel (Qu et al., 2018; Su et al., 2020; Sun and Wang, 2020b; Xu and Wang, 2018; Xu et al., 2019). The asphalt binder molecular structures themselves are therefore of good reliability and reference value. The number of molecules (i.e., the content of the different fractions) is referred to previous research articles (Ding et al., 2021). However, unlike the previously constructed molecular models of asphalt binder, the model of asphalt binder constructed in this study is tetragonal, rather than cubic in shape. Asphalt binder is an amorphous material. Therefore, changes in the shape of the amorphous cells in the simulations do not inherently and seriously affect the accuracy of the final investigation conclusions. The morphological difference of this model is mainly due to the convenience of collecting test data during the direct tensile process. Of course, the reliability of the tetragonal asphalt binder model will still

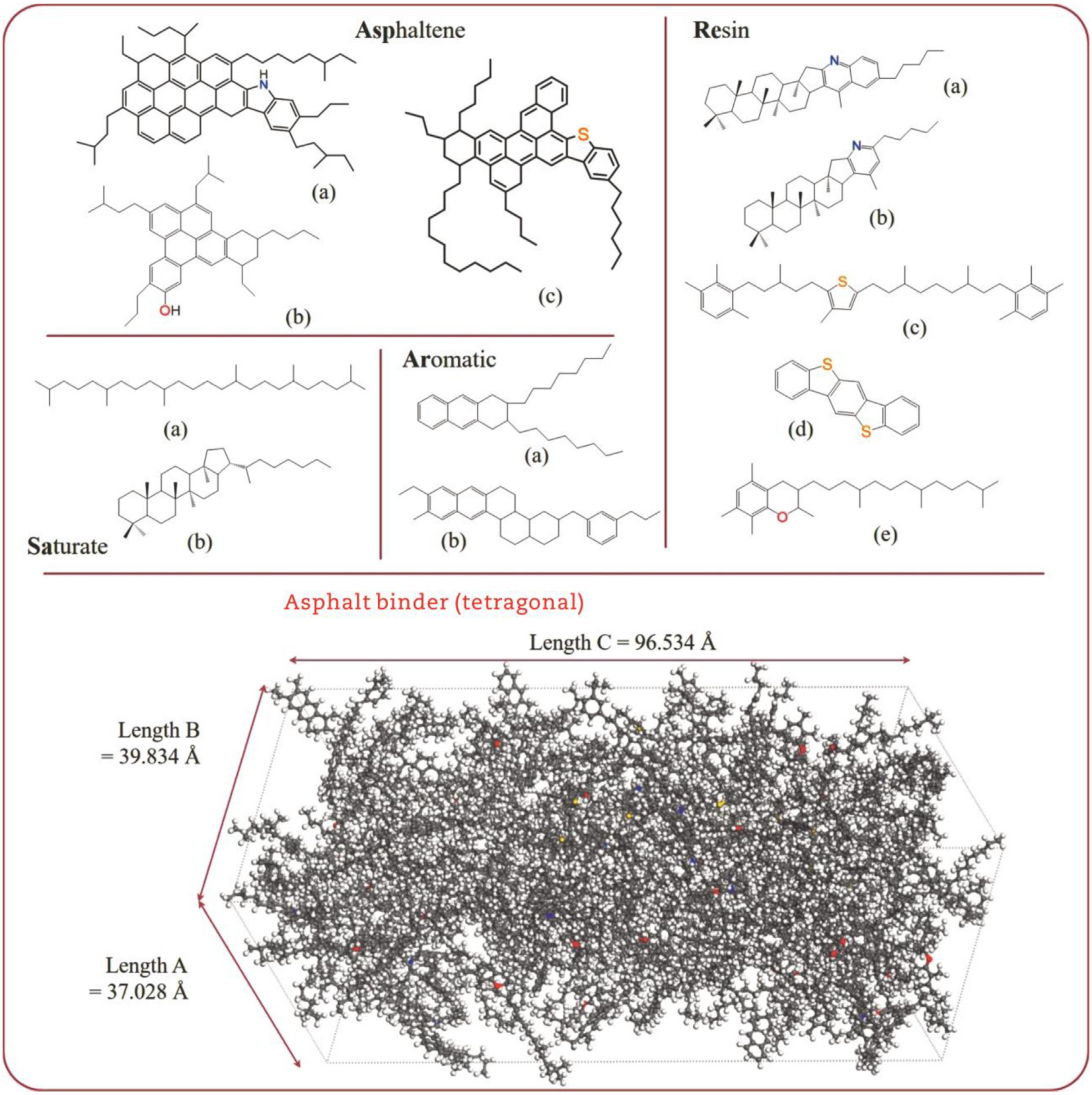

Fig. 1. The tetragonal asphalt binder models for cohesive failure.

be discussed and verified in Section 3.1 of this article.

To fully reflect the attraction and collision effect between molecules in the virtual tensile process, this article expands the number of molecules in the asphalt binder to twice the number of literatures (Huang et al., 2019; Qu et al., 2018), as shown in Table 1.

The weight of asphaltene (Asp), saturate (Sa), aromatic (Ar) and resin (Re) fractions of asphalt binder were 17.8%, 15.5%, 41.4%, and 25.3%, respectively. It is close to other common literatures (Gao et al., 2018; Huang et al., 2019; Yao et al., 2017). All research in this article was completed in Materials Studio® 8.0 simulation platform. The tetragonal asphalt binder model was constructed in Amorphous Cell module. In this article, the initial asphalt binder model is first generated randomly based on Monte Carlo method, which is then put through geometry optimization, molecular dynamics calculation, and annealing simulation to obtain an energy minimized asphalt binder model. Condensed-phase optimized molecular potentials for atomistic simulation studies (COMPASS) forcefields were used in all MD simulations. The temperature of 283 K was used in the geometrical optimization section. 2000 optimization iterations were applied to asphalt binder model and the Ewald and Atom methods were used for electrostatic and van der Waals interactions respectively. The asphalt binder model used an initial random velocity. Nosé & Nosé-Hoover and Berendsen were used as the temperature and pressure control modes for the dynamic calculations. NVT and NPT ensembles were imposed on the dynamic calculations of the asphalt binder model at 283 K. The calculation iterations in the two aforementioned ensemble environments were 200 ps and 300 ps respectively. At 98–598 K, five temperature cycles were used for annealing simulation, and the associated dynamic calculation parameters were the same as those mentioned above. After all the optimization processes have been completed, the stable tetragonal asphalt model can be obtained.

The lattice parameters of tetragonal asphalt model, including length and angle, were obtained by dynamic optimization of the NPT ensemble environment, as shown in Fig. 1. The lattice sizes of tetragonal asphalt model were 37.028 A (Length A), 39.834 A (Length B) and 96.534 A (Length C), respectively. Additionally, the lattice angle of tetragonal asphalt model was fixed at 90° in all directions. Notably, length C was the direction in which the tensile strain was applied.

Table 2
Strain mode of tensile process applied to asphalt binder materials.

Cumulative strain (%)	Strain combination		
5	0.1%-50	0.5%-10	1.0%-5
10	0.1%-100	0.5%-20	1.0%-10
15	0.1%-150	0.5%-30	1.0%-15
20	0.1%-200	0.5%-40	1.0%-20
25	0.1%-250	0.5%-50	1.0%-25
30	0.1%-300	0.5%-60	1.0%-30
40	0.1%-400	0.5%-80	1.0%-40

2.2. *Virtual strain load method applied to asphalt binder*

To study the cohesive damage characteristics of asphalt binders more directly, this article establishes a virtual cumulative strain loading method, i.e., virtual strains are loaded in the Length C direction of the asphalt model. This loading method was designed to simulate the displacement of the fixture at the ends of the asphalt binder specimen during the actual tensile process (e.g., UTM tensile test). By gradually applying minimum strain increment, the relationship between traction stress-traction strain of the asphalt material in the virtual environment was obtained. The virtual strain loading process was controlled by Eq. (1) and the cumulative total strain (i.e., cumulative strain) of the asphalt model was determined by the combination of the minimum strain increment (i.e., strain loading rate) and the number of strain loads (i.e., loading number of strain). Depending on the high, medium, and low strain loading rates, the minimum strain increments are 0.1%, 0.5%, and 1.0%, respectively. The cumulative strain increases from 5% to 40%. The same cumulative strains for different strain loading rates were met for different strain loading numbers, as shown in Table 2.

The virtual cumulative strain loading model proposed in this article was controlled by the custom programming script and was run on Materials Studio® 8.0 simulation platform. After each virtual strain was applied, the asphalt binder model can be re-equilibrated with 100 ps of dynamics under NVT ensemble. The ambient temperature was kept at 283 K. Other dynamic calculation parameters remain the same as described earlier in this article.

$$\delta = N_{\text{strain}} \Delta\delta \tag{1}$$

where δ is the cumulative strain after completing several tensile increments (i.e., cumulative strain), $\Delta\delta$ is the minimum strain increment in a single tensile (i.e., strain loading rate), N_{strain} is the number of stretch during the asphalt binder tensile process (i.e., loading number of strain).

3. Results and discussions

3.1. *Reliability discussion based on thermodynamics and classical mechanics*

To ensure the reliability of models used in this study, thermodynamics and classical mechanical parameters were used to verify the accuracy of this model. Density and glass transition temperature were used as thermodynamic validation indicators. Meanwhile, bulk modulus and Young's modulus were used as validation indicators for classical mechanics.

After the dynamic calculation of 300 ps, the density of tetragonal asphalt binder model reached a steady state. The steady density of asphalt binder was 1.004 g/cm^3 (transverse dashed line in Fig. 2(a)). Based on the van der Waals surface (vdW surface in Fig. 2(a)) of

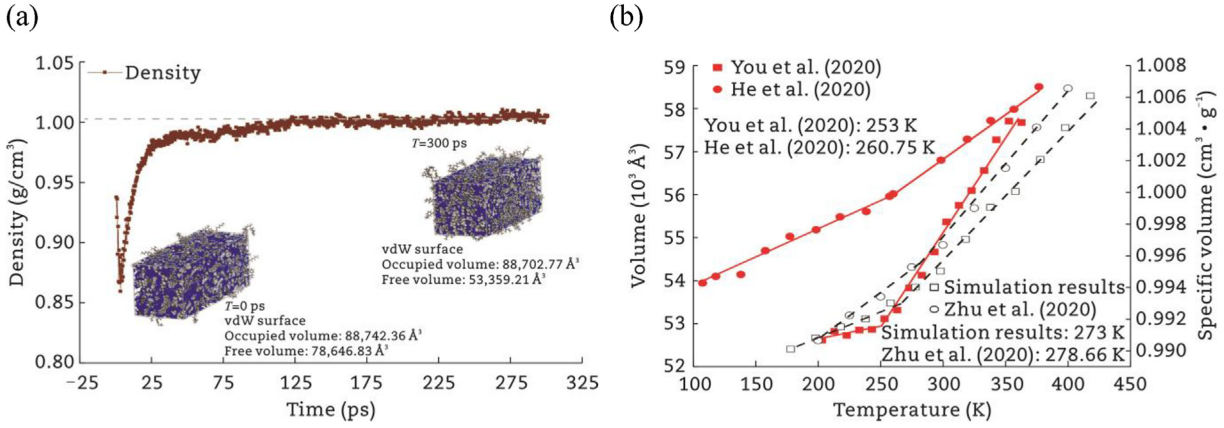

Fig. 2. Thermodynamics reliability analysis of tetragonal asphalt binder. (a) Density. (b) Glass transition temperature.

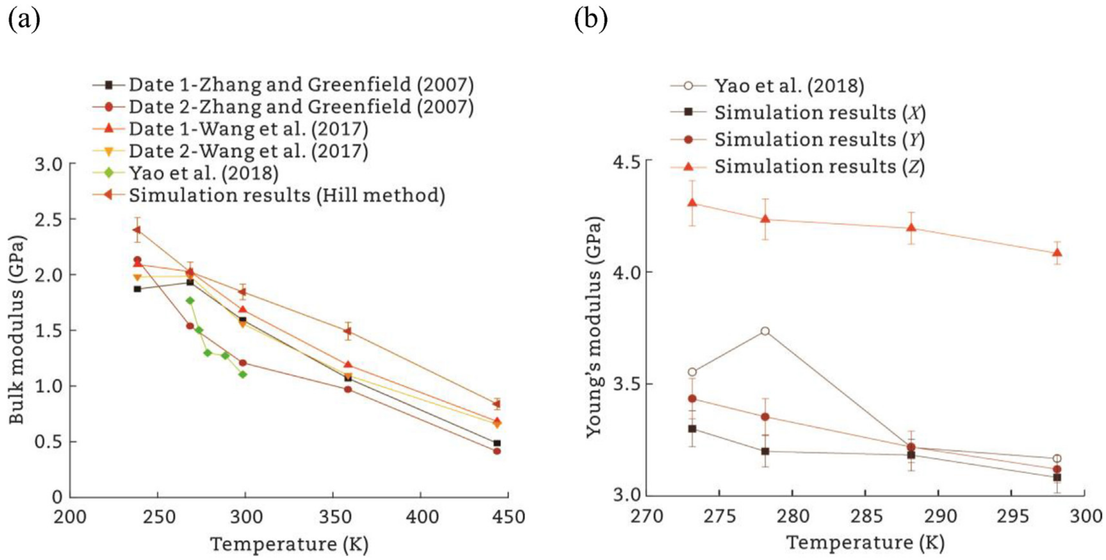

Fig. 3. Classical mechanics analysis of tetragonal asphalt binder. (a) Bulk modulus. (b) Young's modulus.

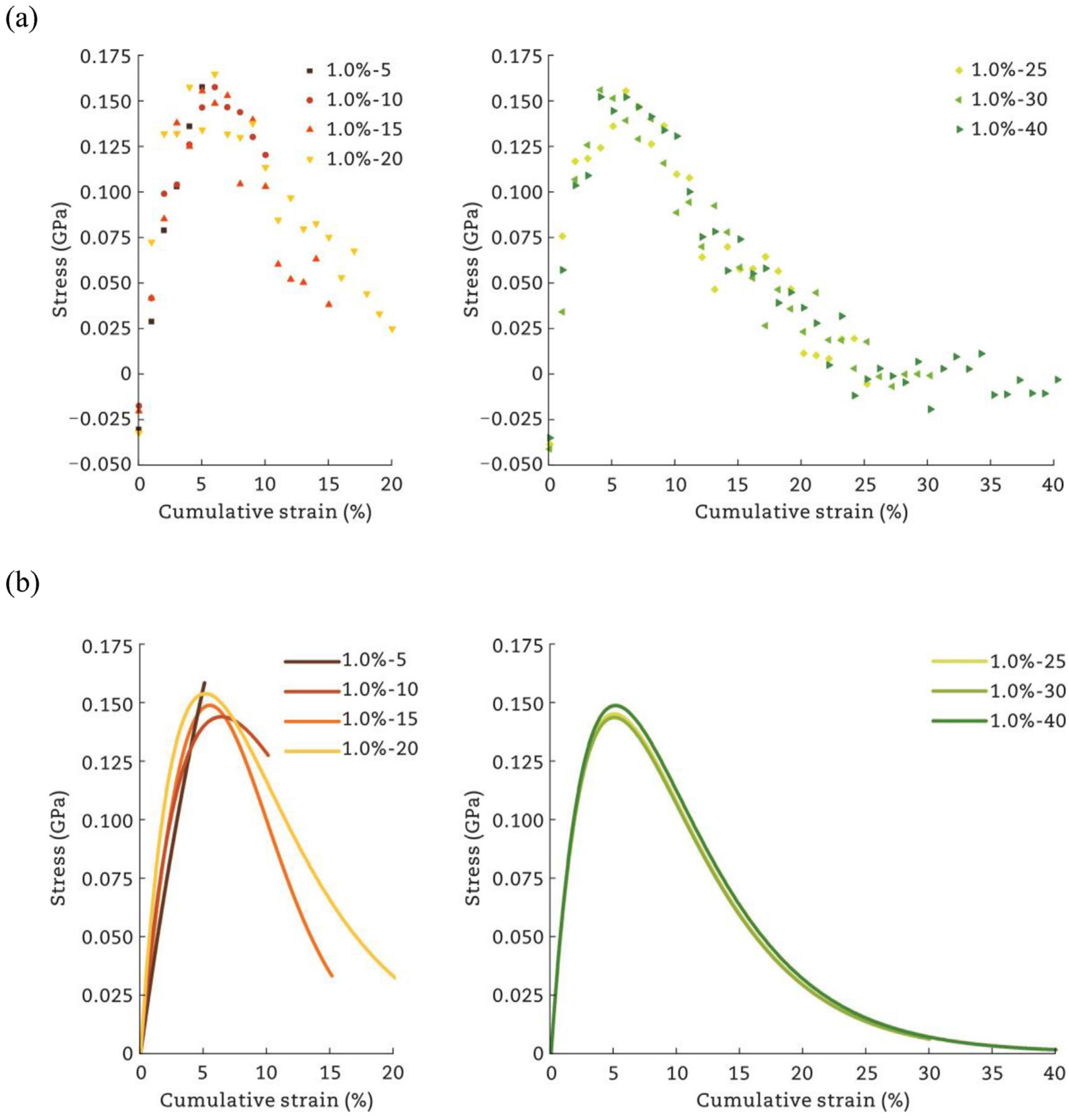

Fig. 4. Traction stress-cumulative strain curve for asphalt binder at 1.0% strain loading rate. (a) Scatter data. (b) Exponential model of cohesion failure.

molecules, the free volume and occupied volume of the asphalt binder model were calculated and visualised. van der Waals surface is the most commonly used molecular volume theory in chemical research (Lu and Chen, 2012; Manzetti and Lu, 2013). The internal volume of the van der Waals surface represents the volume of space occupied by molecules (i.e., occupied volume). Conversely, the space outside the van der Waals surface represents the free volume. The free and occupied volume can be used to analyze the density of amorphous cell under pressure. In the initial state (0–1 ps), the occupied and free volume of the asphalt binder model are 88,742.36 Å^3 and 78,646.83 Å^3, respectively. Dynamic calculation of 300 ps reduced the free volume of the asphalt binder model to 53,359.21 Å^3, a reduction of 32.15%. The occupied volume represented asphalt binder materials were 88,702.77 Å^3, which is close to the initial state. It was indicated that the ambient pressure compressed the free volume of the asphalt binder model, increasing the density of the amorphous cell to satisfy the real test results (LesueurRead and Whiteoak, 2003, 2009). The visualization of the molecular volumes showed the change in free volume being compressed in the asphalt binder model (Fig. 2(a)). A large amount of gradual reduction in the blue portion can be observed on the front and side of the asphalt binder model.

The laboratory test of glass transition temperature is determined with the aid of differential scanning calorimetry (DSC) and dynamic mechanical analysis (DMA) (Khong et al., 1978; Wang et al., 2020; Yadav et al., 2018). The DSC determination of the glass transition temperature is obtained as a change in specific heat capacity (Zhu and Zhou, 2019). In MD, the glass transition temperature is defined in the specific volume (or volume)-temperature transition region. The complete specific volume curve can be divided into two regions: high-temperature region and low-temperature region. The intersection of the high and low temperature regions is the glass transition temperature (T_g). In particular, the glass transition temperature, whether from laboratory tests or simulations, is a temperature region and not a specific value (Chu et al., 2019). A temperature cycle from 178 K to 418 K was applied to the tetragonal asphalt binder model to obtain the glass transition temperature, with reference to the study by You et al. (2020), He et al. (2020), and Zhu et al. (2020). The glass transition temperature of this research was 273 K, as shown in Fig. 2(b). The trend of specific volume (or volume) with temperature was similar when compared to You et al. (2020) and Zhu et al. (2020). The results of the laboratory tests indicated that the glass transition temperature of asphalt binder varied from 223 K to 303 K (Tabatabaee et al., 2012). The results of this research conformed to this law mentioned above.

Reliability verification under classical mechanics conditions is important for the cohesive stress-cumulative strain relationship of asphalt binder. Mechanical modulus parameters are an important way to evaluate the reliability of molecular model for simulation calculations.

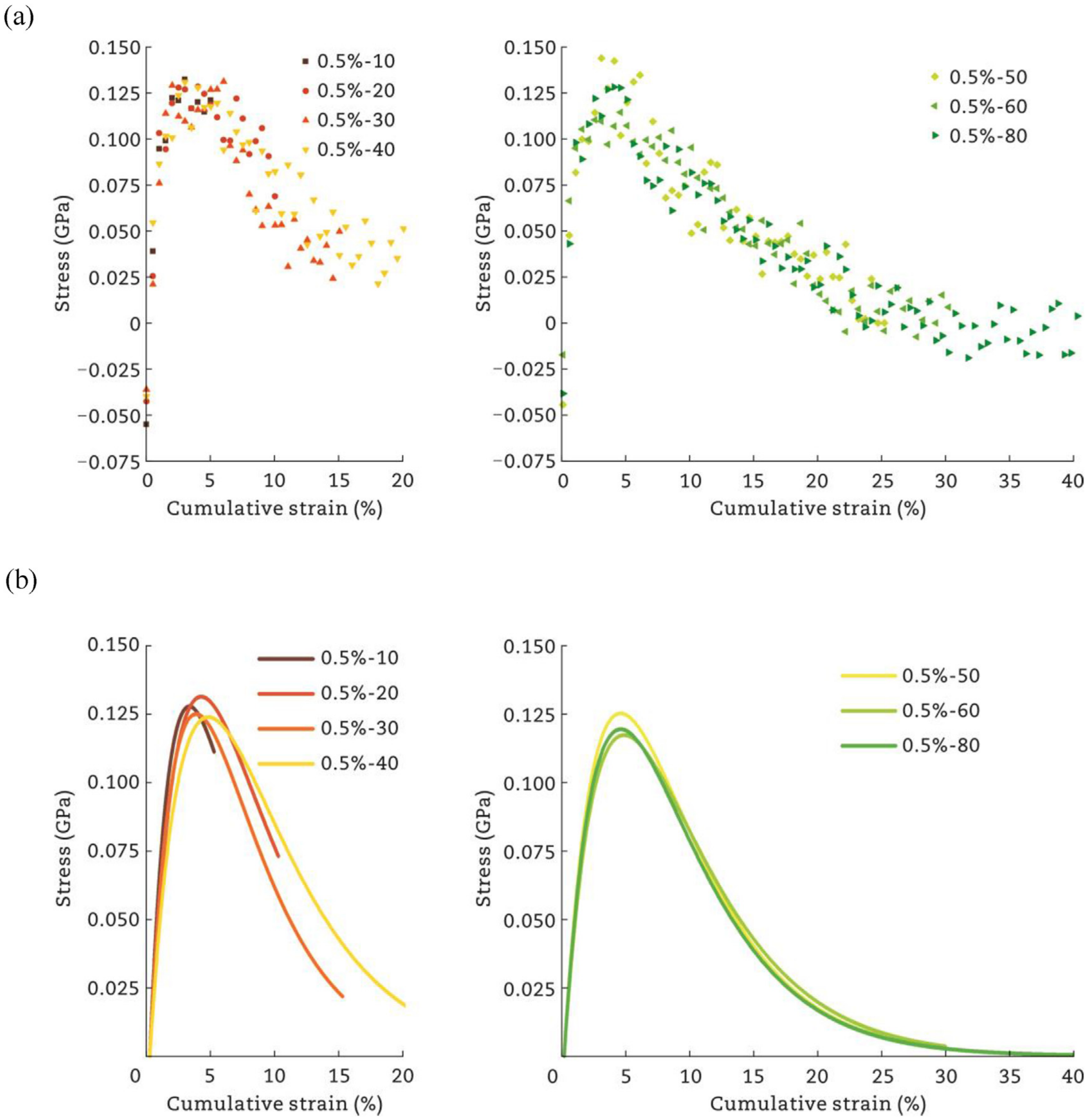

Fig. 5. Traction stress-cumulative strain curve for asphalt binder at 0.5% strain loading rate. (a) Scatter data. (b) Exponential model of cohesion failure.

However, unfortunately, there are no reliable laboratory data available in the literatures to illustrate the modulus-temperature relationship for asphalt binder. Even in the case of simulation data, only a small amount of data is available. In this article, bulk modulus and Young's modulus of asphalt binder were obtained by the constant strain method in the range of 200 K–450 K. The constant strain method estimates the elastic constant matrix by a series of finite difference approximations. The bulk modulus is an evaluation of the ability of materials to resist changes in environmental pressure. Wang et al. (2017), Yao et al. (2018), and Zhang and Greenfield (2007) indicated that the bulk modulus of cubic asphalt binder decreased gradually with increasing temperature (Fig. 3(a)). The bulk modulus used in this article has the same temperature-dependent trend. However, the difference is that the bulk modulus of the tetragonal asphalt binder in this article is higher than the literatures results.

When considering Young's modulus, literatures often treat asphalt binder in a simplified way as anisotropic mechanical response mode (Su et al., 2020; Yao et al., 2018). Furthermore, in the existing literatures, there is no three-directions (*X*, *Y*, and *Z*) data record of Young's modulus, such as Yao et al. (2018). This research provided three-directions modulus data for asphalt binder mode. Yao et al. (2018) indicated that Young's modulus showed a negative correlation with temperature. In all directions, Young's modulus of asphalt binder showed a similar trend. In the *X* and *Y* directions, Young's modulus of the tetragonal asphalt binder was close. However, Young's modulus in the *Z* direction was significantly higher than in the other directions, with the modulus remaining above 4.0 GPa at all temperatures, as shown in Fig. 3(b).

3.2. *Response of strain loading mode: function and analysis*

The relationship of stress-cumulative strain is the main response representation of the stress loading mode. The stress-cumulative strain curves produced by different strain loading modes were not identical. Furthermore, the fitted functions for the stress-strain curves showed valid mathematical representation of the asphalt binder cohesive failure phenomenon. In this section, tensile strain and re-equilibration process were applied to obtain reliable traction stress and critical separation strain in the asphalt binder model. It is worth noting that the separation strain in this research was in the form of cumulative percentages, calculated from the asphalt binder at the initial time when no tension was applied. The expression of cumulative strain provided a further indication of the stress-strain damage relationship. Response data generated by 21 stress loading modes in the range of cumulative strain 5%–40% were included in the statistics.

As standard functions, the exponential cohesion zone model (Eq. (2)) is applied to the fitting of response data. With the aid of parametric fitting, cohesive zone model is able to obtain the maximum traction

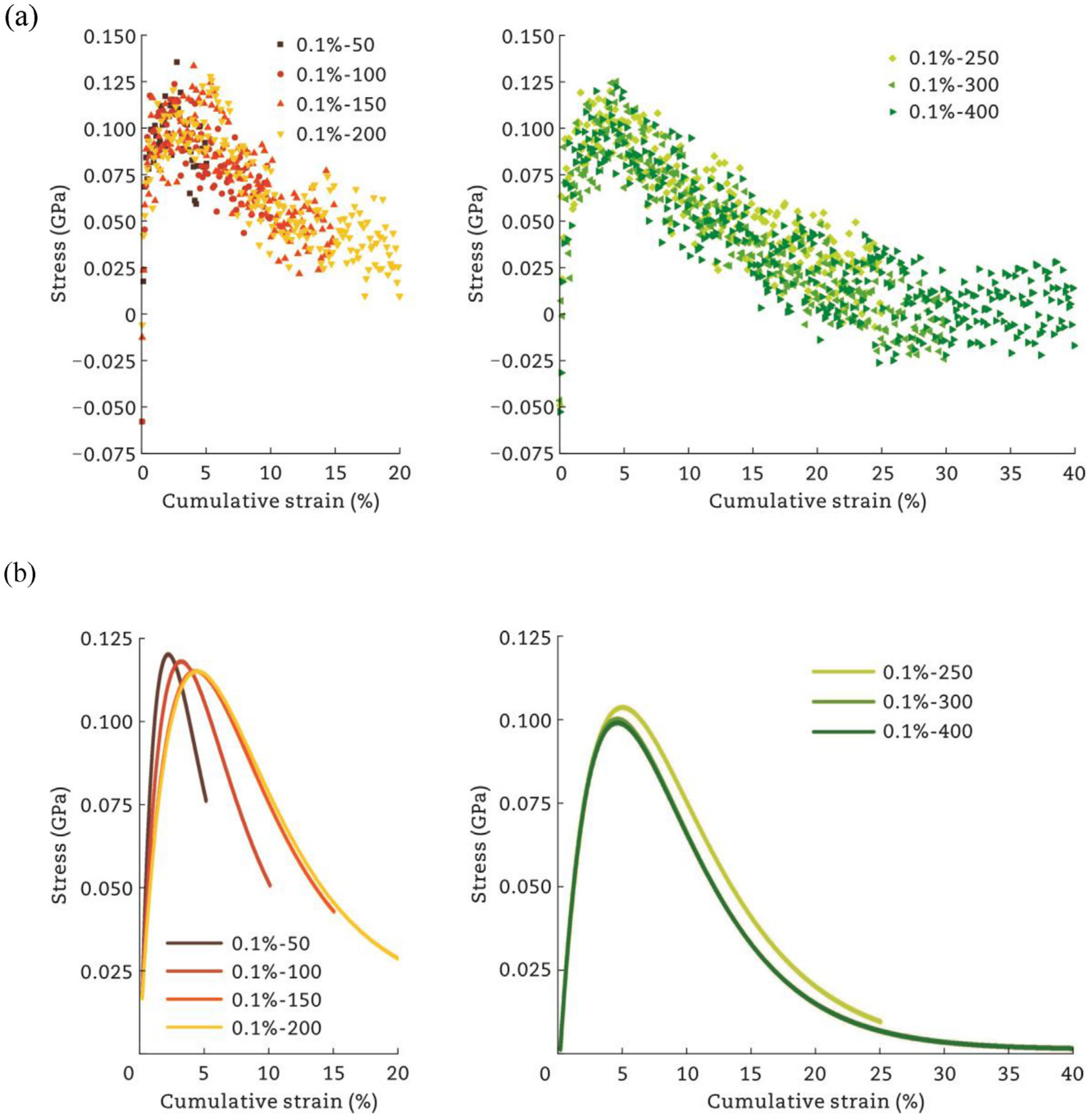

Fig. 6. Traction stress-cumulative strain curve for asphalt binder at 0.1% strain loading rate. (a) Scatter data. (b) Exponential model of cohesion failure.

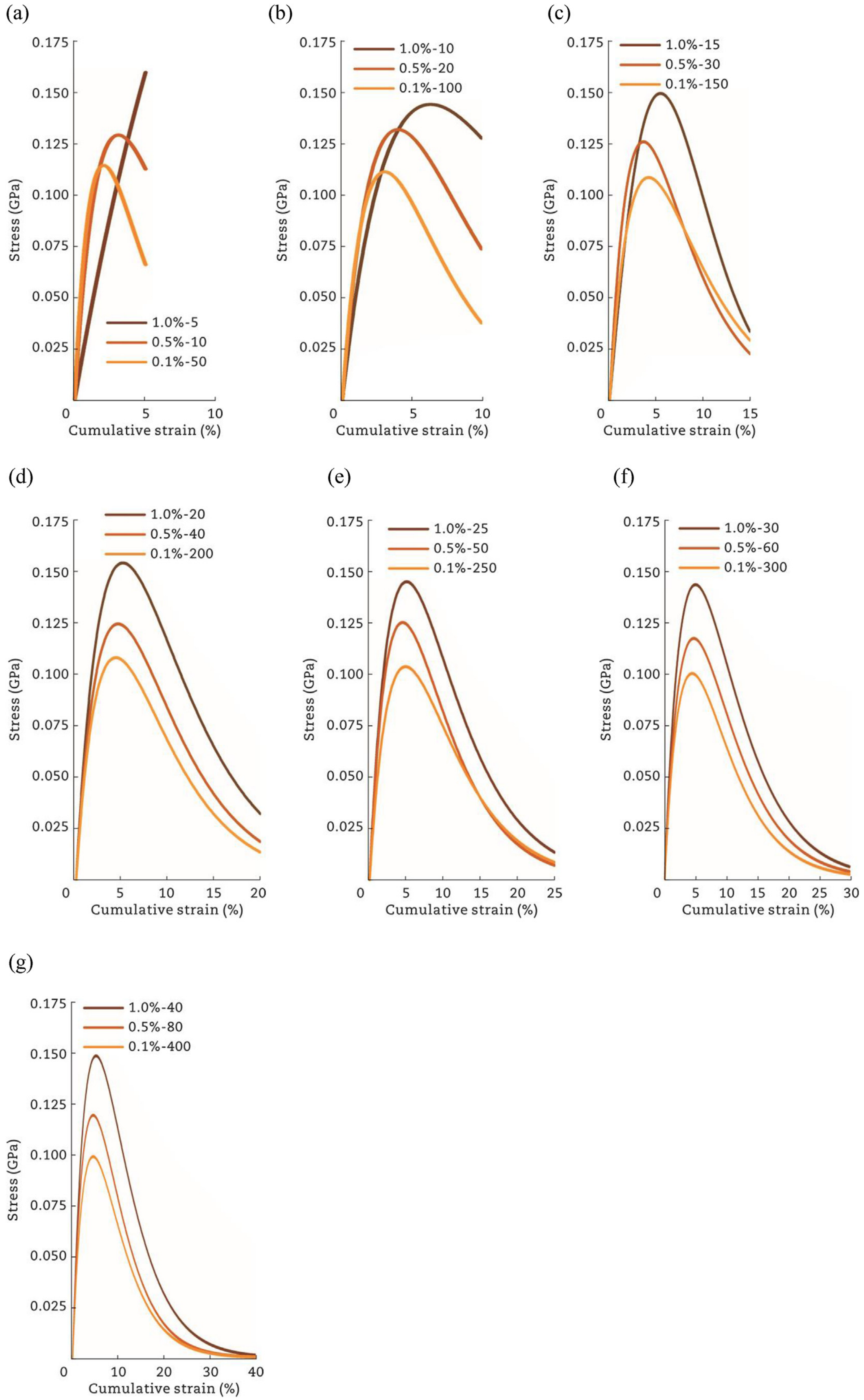

Fig. 7. The influence of cumulative strain on asphalt binder cohesion failure. (a) 5%. (b) 10%. (c) 15%. (d) 20%. (e) 25%. (f) 30%. (g) 40%.

stress, critical separation strain and cohesive failure form for asphalt binder. In the historical literature, the exponential cohesion model has been shown to accurately describe the phenomenon of asphalt binder cohesive failure (Du et al., 2021; Li and Marasteanu, 2005; Sun and Wang, 2020b).

$$\sigma = T_{\mathrm{c}} \frac{\delta}{\delta_{\mathrm{c}}} \exp\left(1 - \frac{\delta}{\delta_{\mathrm{c}}}\right) \tag{2}$$

where σ and δ are the dynamic values of stresses and cumulative strain during the tensile process, respectively, T_{c} is the maximum traction stress before cohesive failure of asphalt binder, δ_{c} is the critical separation strain value at $\sigma = T_{\mathrm{c}}$.

The work of separation can be obtained from traction stress-cumulative strain curve by integral calculation (Eq. (3)). At the same time, the work of separation per area can be solved by introducing the area when asphalt binder cohesive damage occurs.

$$D_{\Gamma} = \frac{\int_0^{\infty} \sigma \mathrm{d}\delta}{A} \tag{3}$$

where D_{r} is the work of separation per area during the tensile process of asphalt binder, A is the average of the area when cohesion failure occurs.

The scatter data and fitted functions for the different strain loading modes are shown in Figs. 4–6. The reliability of all fitted functions is above 65%. Detailed R^2 values and fitted parameters are presented in Appendix. It is worth noting that the removal of anomalous data points is a necessary pre-processing step prior to fitting in order to improve data application and avoid anomalous effect.

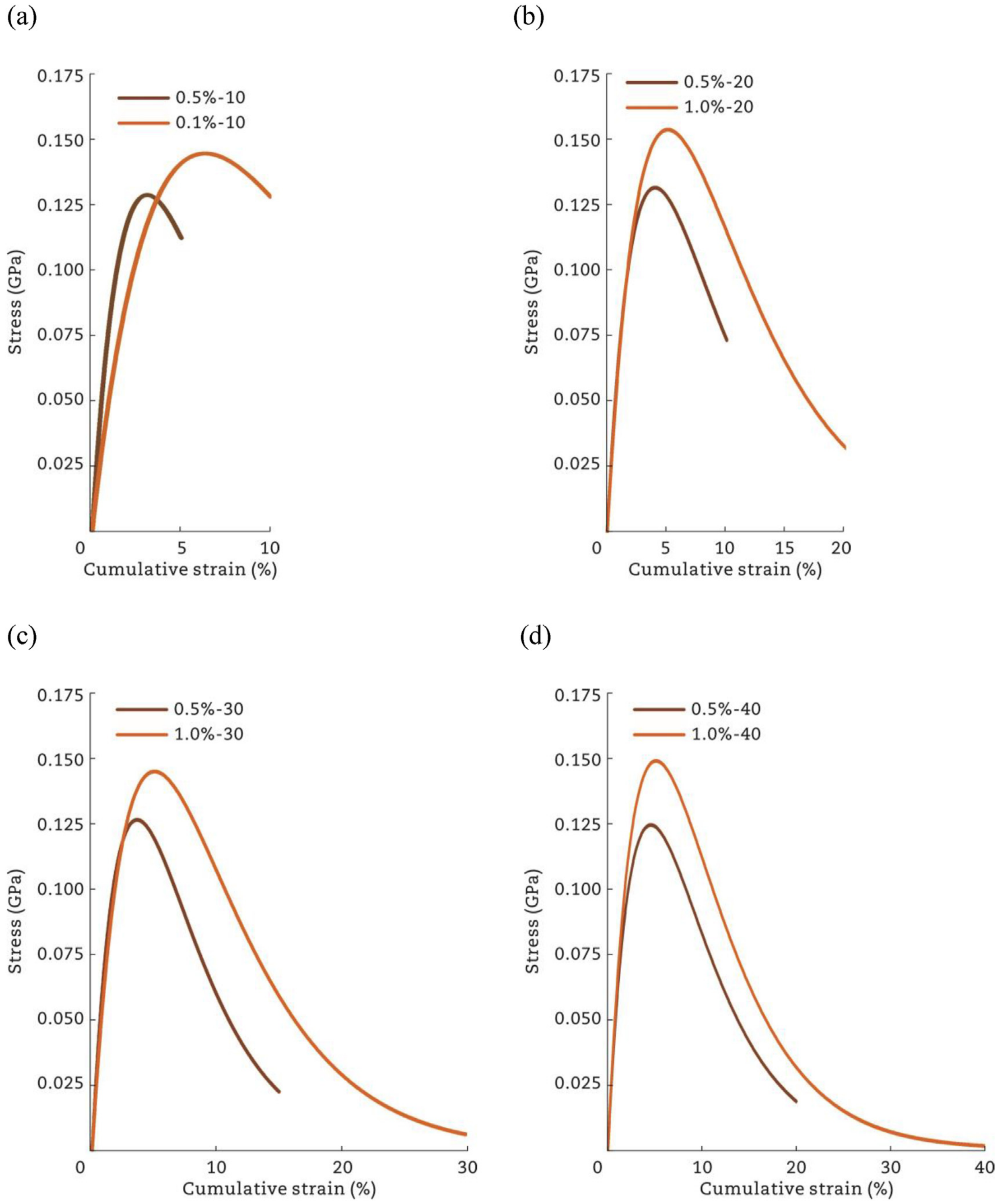

Fig. 8. The influence of loading number of strain on asphalt binder cohesive failure. (a) 10. (b) 20. (c) 30. (d) 40.

3.3. Similarity and continuity in stress-cumulative strain curves

Based on the imposition of multiple stress combination modes in Section 2.2 of this article, this section focuses on the effect of strain loading rate on the form of asphalt binder cohesive failure.

Based on the analysis of the loading results for 21 strain combinations, the scatter trends of the traction stresses within the asphalt binder showed significant overlapping characteristics (Figs. 4(a), 5(a) and 6(a)), and the stress change curves for asphalt binder obtained based on Eq. (2) (proposed in Section 3.2) have a high extent similarity as shown in Figs. 4(b), 5(b) and 6(b). During the initial tensile process, the traction stresses within the asphalt binder quickly climbed to the peak region (i.e., maximum traction stress), and then the stress curve gradually decreased to 0 GPa. After comparing all strain loading combinations, it was found that the maximum traction stress would occur in the range of 2.5%–5.0%. Complete cohesive failure (i.e., 0 traction stress) generally occurs after 25%.

In the high strain rate (1.0%), the short-range (i.e., cumulative strain value less than 20%) of asphalt binder traction stress curve has obvious amplitude fluctuation. The same fluctuation phenomenon occurs at moderate strain rates (0.5%) and low strain rates (0.1%). The maximum traction stress and critical separation strains obtained from the three strain loading rates gradually become stable when the cumulative strain value reaches 25%.

Considering the stability of cohesion failure, 25% cumulative strain value condition was selected as the necessary prerequisite to determine the cohesive failure region (Figs. 4(b), 5(b) and 6(b)). Therefore, under the action of low strain loading rate (0.1%), the maximum traction stress of asphalt binder is 0.10109 GPa (average value), and the corresponding separation strain value is 4.59465% (average value). The cohesive failure regions of moderate (0.5%) and high (1.0%) strain loading rate curves are 0.12077 GPa-4.55046% and 0.14589 GPa-5.03503%, respectively.

The traction stress showed that the long-range (i.e., cumulative strain value more than 20%) of asphalt binder traction stress curve remained coincident (or extremely close to) with the short-range, and then gradually continue with the stress applied numbers, such as 0.1%-250, 0.1%-300, and 0.1%-400. It is noteworthy that, due to the scale effect of molecular dynamics simulation, the stress-cumulative strain curves showed considerable and non-negligible oscillations in some strain combinations, i.e., 0.1%-50 and 0.1%-100. The oscillation effect was related to too low strain loading rate. When the traction stress is detected, the too low strain loading rate makes the traction stress overconsider the chemical bond fracture or atomic movement in the asphalt binder model, even though these were caused by the irregular thermal movement of molecules.

Table 3
The work of separation and multiple ratios under different stress loading combinations.

Loading number of strain	The work of separation D_{r} (J/m^2)	The work of separation per loading number N_{D_r} (J/m^2)	Ratio
0.5%-10	0.617601	0.061760	2.01758
1.0%-10	1.246062	0.124606	
0.5%-20	1.020270	0.051014	1.87996
1.0%-20	1.918070	0.095904	
0.5%-30	1.072837	0.035761	1.89201
1.0%-30	2.029820	0.067661	
0.5%-40	1.134110	0.028353	1.90241
1.0%-40	2.157545	0.053939	

3.4. Dependence and constancy in stress-cumulative strain curves

Under conditions of reaching the same extent of cumulative strain, this section focuses on the analysis of the effect of different stress loading modes on the form of asphalt binder cohesive failure, in particular the maximum traction stress at which cohesive failure occurred. Seven different cumulative strains in the range of 5%–40% were used as control variables for horizontal comparisons during the tensile of the asphalt binder, as shown in Fig. 7. All simulation results showed that the maximum traction stress for asphalt binder tensile failure was reduced as the strain rate declined after the target cumulative strain was reached. The high strain loading rate (1.0%) resulted in a high maximum traction stress (0.14878 GPa) during asphalt binder tensile failure after the same 40% of cumulative strain was reached. And the maximum traction stresses for moderate (0.5%) and low (0.1%) strain rates were 0.11955 and 0.09916 GPa, respectively. The other cumulative strain situations

Table 4
Basic performance indicators of asphalt binder.

Type of asphalt binder	Penetration (0.1 mm, 25 °C 100 g 5 s)	Ductility (cm, 5 cm/min)	Softening point (°C)
Zhenhai 50#	55	62.0 (10 °C) 70.1 (15 °C)	48
PUMA 70#	74	> 100.0 (10 °C) > 100.0 (15 °C)	46
Kunlun 90#	85	> 100.0 (10 °C) > 100.0 (15 °C)	45

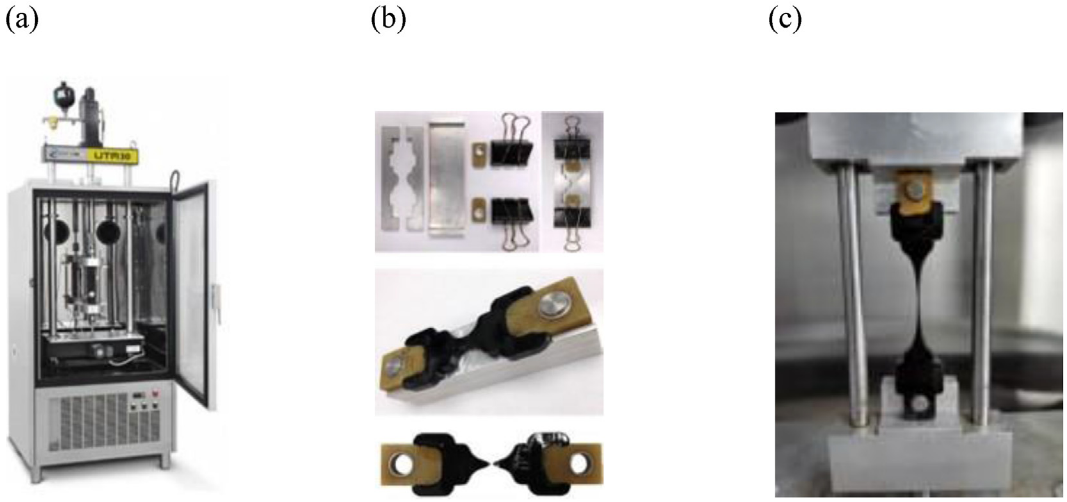

Fig. 9. Cohesion failure of asphalt binder based on BFE method and UTM system. (a) IPC global® UTM-30. (b) Testing moulds in BFE method. (c) Asphalt binder direct tensile damage process in UTM system.

had similar trends. Therefore, the strain loading rate dependence of the maximum traction stress in asphalt binder in tension was reflected in all gradients of cumulative strain change.

It is worth noting that for the loading combination of 1.0%-5 (Fig. 7(a)), the stress-cumulative strain curve only showed an increasing trend without a decreasing trend. This is mainly due to the fact that when cohesive damage occurs in asphalt binder, the corresponding separation strain value happens to be located near 5% (cumulative strain). The maximum cohesive damage stresses produced by this strain loading mode were still higher than for medium and low strain loading rates. This is consistent with the strain loading rate dependence proposed above.

On the other hand, in the process of tensile, the separation strain values corresponding to asphalt binder cohesive failure were constant, especially in the cumulative strain values of 20%, 25%, 30% and 40% (e.g., Fig. 7(d)–(g)). However, the constancy is disturbed to some extent in the cumulative strain values of 5%–15%. In the process of large-range stretch, the cohesive failure of asphalt binder materials occurs smoothly at the atomic level, which is a typical stability failure. However, in the process of short-range stretch, the cohesive failure of asphalt binder is in an extremely unstable state. First, the pre-set tensile strain is close to the potential separation strain value in the process of asphalt binder cohesive failure. The mechanical parameters inevitably interfere with the actual separation strain values. In addition, the random atomic motion and

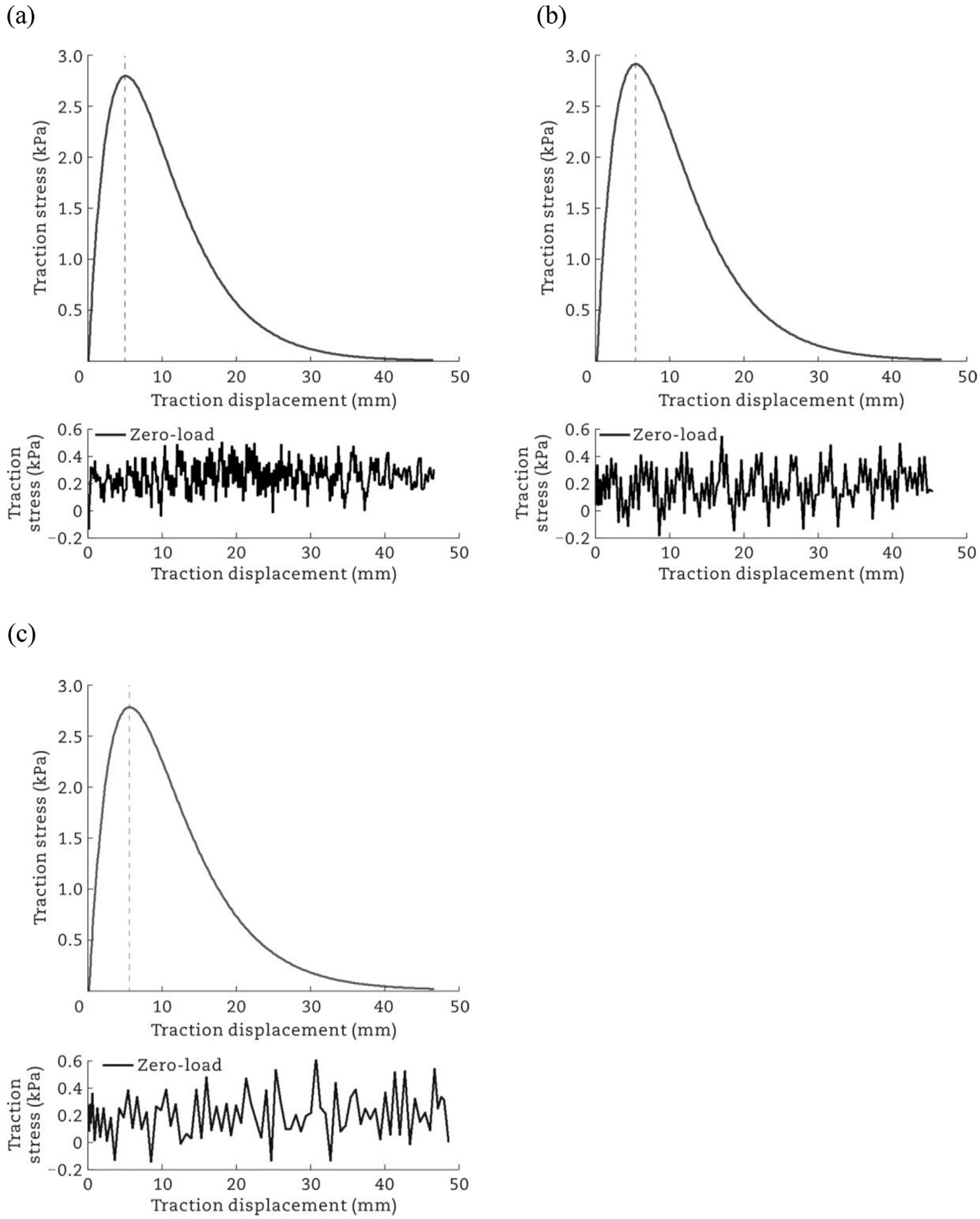

Fig. 10. Asphalt binder tensile damage curve based on UTM system. (a) Zhenhai 50# asphalt binder. (b) PUMA 70# asphalt binder. (c) Kunlun 90# asphalt binder.

chemical bond fracture behavior have more obvious effects on the potential separation strain values during asphalt binder cohesive failure. This effect was reduced to a minimum level during the large-range stretch of asphalt binder.

3.5. *Work of separation contained in loading number of strain*

This section focuses on analysing the dependence of separation work on strain loading number or strain loading rate. This is an energy angle analysis of the stress loading modes effect. In the strain range of 5%–40%, 10, 20, 30, and 40 loading numbers of strain were screened as separation work per loading number for the analysis. In addition, the complete form of asphalt binder cohesive damage was used as a prerequisite for data screening.

Four types of loading number of strain were shown in Fig. 8 in a side-by-side comparison. The overall trend showed that the high strain rate curve is generally higher than the low strain rate. The work of separation per loading number, based on the calculation method presented in Section 3.2, was shown in Table 3. In horizontal comparison, as the loading number of strain increased, the work of separation per loading number decreased from 0.061760 to 0.028353 J/m^2 at 0.5% strain loading rate. It was indicated that the work of separation per loading number decreased as the loading number of strain loaded increased. This mode was similarly expressed in the strain rate of 1.0%. At 10 loading number of strain, the work of separation per loading number at 1.0% (strain loading rate) is 2.01758 times greater than that at 0.5% (strain loading rate). Similarly, the ratios for 20, 30, and 40 loading numbers were 1.87996, 1.89201, and 1.90241, respectively, very close to the two-fold relationship. The two-fold difference regarding the strain loading rate directly contributes to the two-fold relationship for the work of separation per loading number (2-fold). Furthermore, the ratio of work of separation per loading number gradually approached 2-fold as the number of strain loading increased. This was mainly due to the fact that a longer number of strain loading reduced the size effect at the atomic level.

3.6. *Applicability verification based on UTM test*

To verify the applicability of asphalt binder cohesion failure model at the macroscopic scale, the traction stress-traction strain curves of Zhenhai 50#, PUMA 70# and Kunlun 90# asphalt binder were tested by UTM system in this section (Fig. 9). The basic performance indicators of asphalt binder were showed in Table 4. It is important to note that before formally testing the traction stress curve of the asphalt binder, the fluctuation curve of the instrument needs to be obtained first at zero load. This is mainly to exclude signal acquisition errors caused by instrument vibration, as shown in Fig. 10. At zero load, the instrument error generated by UTM system itself was in the range of 0–0.6 kPa.

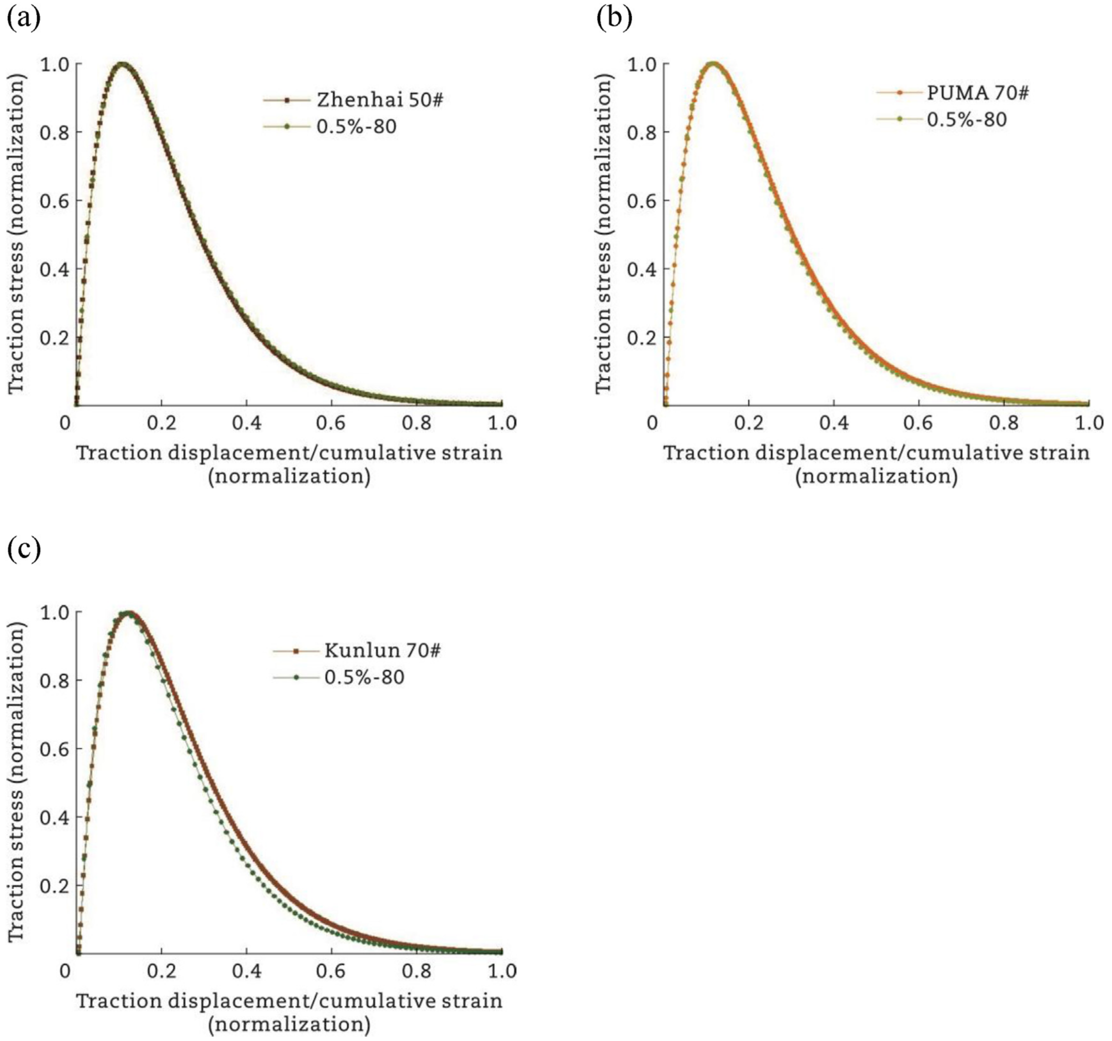

Fig. 11. High similarity of traction stress curves in MD simulations and UTM results. (a) Zhenhai 50# asphalt binder. (b) PUMA 70# asphalt binder. (c) Kunlun 90# asphalt binder.

Combined with the exponential cohesion zone model, the traction stress-traction strain curves and the corresponding key failure parameters (T_c, δ_c) for three types of asphalt binder during direct tension were shown in Fig. 10 and Table A2. The degree of reliability (R^2) of key failure parameters in cohesion zone model is above 0.85, therefore the fitted curves have good accuracy. The curves showed that there was no dependence between the morphology of traction stress curves and the type of asphalt binder. The morphology of traction stress curves for the three types of asphalt binder showed a typical single-peaked form. During the process of tension, the traction stress increased rapidly to the peak region and then slowly decreases to 0 kPa. The appearance of the peak region indicated that cohesive damage has occurred in asphalt binder. The maximum traction stress can be considered to represent the maximum cohesive strength of asphalt binder, which was mainly for resistance to external tensile force. The maximum traction stresses exhibited during tension were 2.80112 kPa, 2.90612 kPa, and 2.78023 kPa for each of the three types of asphalt binder (vertical dashed line in Fig. 10).

The two types of traction stress curves are at different test scales, and therefore MD simulation results and UTM test results were normalized [0, 1] in this section. The normalization removes the influence of the magnitude of observed quantities. After comparing and filtering the normalized curves for 21 strain loading combinations, the strain combination of 0.5%-80 showed the highest similarity to the UTM normalized results for all types of asphalt binder, as shown in Fig. 11. The similarity between MD simulations and UTM results was near perfect for Zhenhai 50# and PUMA 70# asphalt binder, although there were some deviations in the similarity for Kunlun 90# asphalt binder.

4. Conclusions

In this research, the tetragonal asphalt binder model was used as the research object of cohesive failure, and the internal traction stress curve was obtained at atomic level by constant strain method. The effects of three parameter variables of strain loading rate, number of strain loading and cumulative strain on asphalt binder cohesive failure modes were expounded. Relevant conclusions in this research were summarized as follows.

- Thermodynamic verification indicators showed that the tetragonal asphalt binder model constructed in this study was close to the data presented in laboratory or other simulation results. The bulk modulus and Young's modulus obtained were close to the presented literature data. A variety of indicators verified that the asphalt binder models proposed in this research has a high extent of reasonability and applicability, although the asphalt binder model used is different from conventional research.
- With the constant strain loading method, this research was obtained the traction stress-cumulative strain curve of asphalt binder cohesive failure under various parameter states. The cohesive failure region (maximum traction stress-critical separation strain) was obtained based on the exponential cohesion zone model as the standard function. The work of separation per area was the most important evaluation indicator used in this study. The interfacial area was introduced to realize the surface area density conversion of asphalt binder cohesive strength.
- Similarity and continuity are the most prominent mechanical characteristics of traction stress-cumulative strain curves in asphalt binder. The results of 21 strain combinations showed that the high similarity in stress variation forms and failure area. The continuity was reflected in the fact that the long-range traction stress curve can almost perfectly contain the stress trajectory obtained by short-range tensile. The maximum traction stress often occurs in 2.5%–5.0% of cumulative strain. Complete cohesive destruction generally occurs after 25%. Increasing the tensile number or decreasing the strain rate can effectively limit the oscillation effect in the simulation.
- After reaching the target cumulative strain, the maximum traction stress of cohesive damage of asphalt binder decreases with the decrease of strain rate. Higher strain loading rates correspond to higher maximum cohesion stress. This is a typical dependence on the maximum traction stress-strain loading rate for tensile processes. In addition, the separation strain values corresponding to the cohesive failure of asphalt binders showed a constant characteristic during the tensile process, especially during large-range tensile process, such as cumulative strain values of 20%, 25%, 30%, and 40%. The tensile process of short-range can also show some extent stability, but the influence of random atomic motion and chemical bond fracture behavior cannot be ignored.
- The dependence around the separation work is an important energy analysis of the effect of stress loading patterns. The cohesive failure of asphalt binder showed that the separation work per loading number decreased gradually with the increase of loading number at the same loading rate. Horizontal comparison of the work of separation per loading number under the same condition showed a significant twofold relationship between the two loading rates (0.5% and 1.0%). That is, 1.0% corresponds to twice the work of separation per loading number of 0.5%. This is apparently due to a twofold difference in strain loading rates.
- Traction stress-traction displacement curves were obtained for Zhenhai 50#, PUMA 70# and Kunlun 90# asphalt binder in UTM system. The test results for all asphalt binder samples showed that the traction stress curve was independent of the type of asphalt binder. The traction stress of the asphalt binder increased rapidly with increasing traction displacement to the peak region. After the peak region, the traction stress slowly decreased to 0 kPa. Normalization is an important way of establishing macro and micro-scale correlations for direct tensile testing. After normalization of MD simulation and UTM test results, the traction stress curve represented by 0.5%-80 was highly coincident with the real tensile data. This situation indicated that the virtual strain loading method was able to express the tensile properties of real asphalt binder well, after excluding the effects of unit magnitudes.

Declaration of competing interest

Hainian Wang and Zhen Leng are editorial board members of Journal of Road Engineering and were not involved in the editorial review or the decision to publish this article. All authors declare that there are no competing interests.

Acknowledgments

The work described in this article is supported by the National Key Research and Development Program of China (No. 2021YFB2601000), the National Natural Science Foundation of China (No. 51878063, No. 52078048, and No. 52008029), and the Fundamental Research Funds for the Central Universities, CHD (300102213504).

Appendix

This supporting material is an auxiliary and supportive addition to the research findings about the main article. It mainly includes the mathematical models and key original data from the main article. This material is indexed in Section 3.2 of the main article. Related technical questions can be addressed to the first author.

The exponential cohesion zone model used in Section 3.2 and Section 3.6 of the main article is shown in Eq. (1). The key parameters obtained based on this function, i.e., the maximum traction stress (T_c), the critical separation strain value (δ_c) and the fitting evaluation parameter (R^2) are shown in Tables A1 and A2.

Table A1
Key parameters obtained for 21 strain loading combinations.

Strain loading combination	Mode of cohesion failure (T_c; δ_c)	R^2 (adjusted)
0.1%-50	0.11337 ± 0.00357 2.04217 ± 0.01354	0.65335
0.1%-100	0.11105 ± 0.00333 3.04791 ± 0.00253	0.65149
0.1%-150	0.10789 ± 0.00536 4.15141 ± 0.00862	0.66023
0.1%-200	0.10778 ± 0.00251 4.31448 ± 0.00529	0.70598
0.1%-250	0.10382 ± 0.00236 4.85838 ± 0.00313	0.72548
0.1%-300	0.10028 ± 0.00180 4.45306 ± 0.01012	0.85004
0.1%-400	0.09916 ± 0.00215 4.47251 ± 0.00258	0.88798
0.5%-10	0.12812 ± 0.00725 3.08312 ± 0.44508	0.87098
0.5%-20	0.13167 ± 0.00513 3.99869 ± 0.24126	0.82097
0.5%-30	0.12531 ± 0.00475 3.60149 ± 0.14722	0.86661
0.5%-40	0.12421 ± 0.00473 4.55050 ± 0.18369	0.78796
0.5%-50	0.12534 ± 0.00507 4.45747 ± 0.18276	0.81763
0.5%-60	0.11742 ± 0.00372 4.72176 ± 0.15046	0.88632
0.5%-80	0.11955 ± 0.00404 4.47216 ± 0.15152	0.89047
1.0%-5	0.31683 ± 0.33021 21.54021 ± 27.60800	0.94893
1.0%-10	0.14399 ± 0.00368 6.33731 ± 0.42522	0.96262
1.0%-15	0.15008 ± 0.00741 5.02312 ± 0.10858	0.89494
1.0%-20	0.15389 ± 0.00510 5.07076 ± 0.18445	0.92482
1.0%-25	0.14521 ± 0.00608 5.00382 ± 0.21524	0.90781
1.0%-30	0.14369 ± 0.00514 5.00386 ± 0.18065	0.93752
1.0%-40	0.14878 ± 0.00480 5.09741 ± 0.16489	0.94893

Table A2
Key failure parameters based on UTM system.

Type of asphalt binder	Mode of cohesion failure (T_c; δ_c)	R^2 (adjusted)
Zhenhai 50#	2.80112 ± 0.01010 5.01210 ± 0.12071	0.88456
PUMA 70#	2.90612 ± 0.09810 5.21210 ± 0.13001	0.89008
Kunlun 90#	2.78023 ± 0.01010 5.45510 ± 0.10991	0.88123

References

Chu, L., Luo, L., Fwa, T.F., 2019. Effects of aggregate mineral surface anisotropy on asphalt-aggregate interfacial bonding using molecular dynamics (MD) simulation. Construction and Building Materials 225, 1–12.

Ding, H., Wang, H., Qu, X., et al., 2021. Towards an understanding of diffusion mechanism of bio-rejuvenators in aged asphalt binder through molecular dynamics simulation. Journal of Cleaner Production 299, 126927.

Ding, G., Yu, X., Dong, F., et al., 2020. Using silane coupling agent coating on acidic aggregate surfaces to enhance the adhesion between asphalt and aggregate: a molecular dynamics simulation. Materials 13 (23), 5580.

Du, Z., Zhu, X., 2019. Molecular Dynamics simulation to investigate the adhesion and diffusion of asphalt binder on aggregate surfaces. Transportation Research Record 2673, 500–512.

Du, Z., Zhu, X., Li, F., et al., 2021. Failure of the asphalt-aggregate interface under tensile stress: insight from molecular dynamics. Journal of Materials in Civil Engineering 33 (3), 04021008.

Feng, P., Wang, H., Ding, H., et al., 2020. Effects of surface texture and its mineral composition on interfacial behavior between asphalt binder and coarse aggregate. Construction and Building Materials 262, 120869.

Gao, Y., Zhang, Y., Gu, F., et al., 2018. Impact of minerals and water on bitumen-mineral adhesion and debonding behaviours using molecular dynamics simulations. Construction and Building Materials 171, 214–222.

Gong, Y., Xu, J., Yan, E., 2021. Intrinsic temperature and moisture sensitive adhesion characters of asphalt-aggregate interface based on molecular dynamics simulations. Construction and Building Materials 292, 123462.

He, L., Li, G., Lv, S., et al., 2020. Self-healing behavior of asphalt system based on molecular dynamics simulation. Construction and Building Materials 254, 119225.

Huang, M., Zhang, H., Gao, Y., et al., 2019. Study of diffusion characteristics of asphalt-aggregate interface with molecular dynamics simulation. International Journal of Pavement Engineering 22 (3), 319–330.

Khong, T.D., Malhotra, S.L., Blanchard, L.P., 1978. A study of the glass transition temperature of asphalts and their viscosity. Rheologica Acta 17 (6), 654–662.

Lesueur, D., 2009. The colloidal structure of bitumen: consequences on the rheology and on the mechanisms of bitumen modification. Advances in Colloid and Interface Science 145 (1–2), 42–82.

Li, D.D., Greenfield, M.L., 2014. Chemical compositions of improved model asphalt systems for molecular simulations. Fuel 115, 347–356.

Li, X., Marasteanu, M.O., 2005. Cohesive modeling of fracture in asphalt mixtures at low temperatures. International Journal of Fracture 136 (1), 285–308.

Liu, J., Yu, B., Hong, Q., 2020. Molecular dynamics simulation of distribution and adhesion of asphalt components on steel slag. Construction and Building Materials 255, 119332.

Lu, T., Chen, F., 2012. Quantitative analysis of molecular surface based on improved Marching Tetrahedra algorithm. Journal of Molecular Graphics and Modelling 38, 314–323.

Luo, L., Chu, L., Fwa, T.F., 2020. Molecular dynamics analysis of moisture effect on asphalt-aggregate adhesion considering anisotropic mineral surfaces. Applied Surface Science 527, 146830.

Manzetti, S., Lu, T., 2013. The geometry and electronic structure of Aristolochic acid: possible implications for a frozen resonance. Journal of Physical Organic Chemistry 26 (6), 473–483.

Martín-Martínez, F.J., Fini, E.H., Buehler, M.J., 2015. Molecular asphaltene models based on Clar sextet theory. RSC Advances 5 (1), 753–759.

Qu, X., Liu, Q., Guo, M., et al., 2018. Study on the effect of aging on physical properties of asphalt binder from a microscale perspective. Construction and Building Materials 187, 718–729.

Ramezani, M.G., Rickgauer, J., 2020. Understanding the adhesion properties of carbon nanotube, asphalt binder, and mineral aggregates at the nanoscale: a molecular dynamics study. Petroleum Science and Technology 38 (1), 28–35.

Read, J., Whiteoak, D., 2003. The Shell Bitumen Handbook, fifth ed. ICE Publishing, London.

Su, M., Si, C., Zhang, Z., et al., 2020. Molecular dynamics study on influence of nano-ZnO/SBS on physical properties and molecular structure of asphalt binder. Fuel 263, 116777.

Sun, W., Wang, H., 2020a. Molecular dynamics simulation of diffusion coefficients between different types of rejuvenator and aged asphalt binder. International Journal of Pavement Engineering 21 (8), 966–976.

Sun, W., Wang, H., 2020b. Self-healing of asphalt binder with cohesive failure: insights from molecular dynamics simulation. Construction and Building Materials 262, 120538.

Tabatabaee, H.A., Velasquez, R., Bahia, H.U., 2012. Predicting low temperature physical hardening in asphalt binders. Construction and Building Materials 34, 162–169.

Tan, Y., Guo, M., 2013. Using surface free energy method to study the cohesion and adhesion of asphalt mastic. Construction and Building Materials 47, 254–260.

Wang, H., Ding, H., Feng, P., et al., 2020. Advances on molecular simulation technique in asphalt mixture. Journal of Traffic and Transportation Engineering 20 (2), 1–14.

Wang, H., Lin, E., Xu, G., 2017. Molecular dynamics simulation of asphalt-aggregate interface adhesion strength with moisture effect. International Journal of Pavement Engineering 18 (5), 414–423.

Xu, G., Wang, H., 2016a. Molecular dynamics study of interfacial mechanical behavior between asphalt binder and mineral aggregate. Construction and Building Materials 121, 246–254.

Xu, G., Wang, H., 2016b. Study of cohesion and adhesion properties of asphalt concrete with molecular dynamics simulation. Computational Materials Science 112, 161–169.

Xu, G., Wang, H., 2018. Diffusion and interaction mechanism of rejuvenating agent with virgin and recycled asphalt binder: a molecular dynamics study. Molecular Simulation 44 (17), 1433–1443.

Xu, M., Yi, J., Feng, D., et al., 2019. Diffusion characteristics of asphalt rejuvenators based on molecular dynamics simulation. International Journal of Pavement Engineering 20 (5), 615–627.

Yadav, A., Kumar, A., Singh, P.K., et al., 2018. Glass transition temperature of functionalized graphene epoxy composites using molecular dynamics simulation. Integrated Ferroelectrics 186 (1), 106–114.

Yao, H., Dai, Q., You, Z., et al., 2017. Property analysis of exfoliated graphite nanoplatelets modified asphalt model using molecular dynamics (MD) method. Applied Sciences 7 (1), 7010043.

Yao, H., Dai, Q., You, Z., et al., 2018. Modulus simulation of asphalt binder models using molecular dynamics (MD) method. Construction and Building Materials 162, 430–441.

You, L., Spyriouni, T., Dai, Q., et al., 2020. Experimental and molecular dynamics simulation study on thermal, transport, and rheological properties of asphalt. Construction and Building Materials 265, 120358.

Yuan, Y., Zhu, X., Chen, L., 2020. Relationship among cohesion, adhesion, and bond strength: from multi-scale investigation of asphalt-based composites subjected to laboratory-simulated aging. Materials and Design 185, 108272.

Zhang, L., Greenfield, M.L., 2007. Analyzing properties of model asphalts using molecular simulation. Energy and Fuels 21 (3), 1712–1716.

Zhu, X., Du, Z., Ling, H., et al., 2020. Effect of filler on thermodynamic and mechanical behaviour of asphalt mastic: a MD simulation study. International Journal of Pavement Engineering 21 (10), 1248–1262.

Zhu, J., Zhou, C., 2019. Rationality evaluation index of asphalt molecular model. Materials Research Express 6 (11), 115110.

Dr. Hainian Wang is currently serving as the principle for Chang'an Dublin International College of Transportation, and professor at Chang'an University. He has been engaged in teaching and research work in the field of road engineering for more than 15 years. His research fields include design theory and methods of regionally special road engineering, road material microstructure characterization and modeling, sustainable paving materials development and evaluation. He published around 160 papers in international and Chinese academic journals.